LSTM-Based Trajectory and Phase-Shift Prediction for RSMA Networks Assisted by AIRS

Brena Kelly Sousa Lima, João Pedro Matos-Carvalho, Rui Dinis, *Senior Member, IEEE*, Daniel Benevides da Costa, *Senior Member, IEEE*, Marko Beko, and Rodolfo Oliveira, *Senior Member, IEEE*

***Abstract*— This paper investigates rate-splitting multiple access (RSMA) networks with multiusers assisted by aerial intelligent reflecting surfaces (AIRS). To improve the sum-rate of the system, the UAV's trajectory and phase-shift vectors are optimized, in which the mobility scenarios with static and dynamic users are explored. In particular, long short-term memory (LSTM)-based frameworks for predicting the UAV's trajectory and the phase-shift of the reflecting elements of AIRS are proposed. For more insight, a third model is created by combining information from the static and dynamic scenarios. Furthermore, to improve the transmit beamforming at the BS, an algorithm based on alternating optimization (AO) under the assumptions of imperfect successive interference cancelation (SIC) is presented. Training progress and testing results are provided to demonstrate the efficiency of the proposed models. In addition, numerical simulations are presented to verify the performance gains in terms of sum-rate. The simulation results show that the UAV performs better in trajectory prediction and phase-shift when different investigated scenarios are not combined.**

***Index Terms*— Intelligent reflecting surface (IRS), long short-term memory (LSTM), rate-splitting multiple access (RSMA), trajectory optimization, precoder design, unmanned aerial vehicle (UAV).**

Manuscript received 3 January 2024; revised 1 April 2024; accepted 22 May 2024. Date of publication 30 May 2024; date of current version 14 November 2024. This work is funded by Fundação para a Ciência e Tecnologia under the project UIDB/50008/2020, UIDB/04111/2020, CEECINST/00147/2018/CP1498/CT0015, as well as Instituto Lusófono de Investigação e Desenvolvimento (ILIND) under Project COFAC/ILIND/COPELABS/1/2022. This research was partially funded by the European Union's Horizon Europe Research and Innovation Programme under the Marie Skłodowska-Curie grant agreement No. 101086387 and by ROBUST under Grant EXPL/EEI-EEE/0776/2021. An earlier version of this paper was presented in part at the IEEE Latin-American Conference on Communications (LATINCOM), Rio de Janeiro, Brazil, December 2022. The associate editor coordinating the review of this article and approving it for publication was Z. Qin. *(Corresponding author: Brena Kelly Sousa Lima.)*

Brena Kelly Sousa Lima is with COPELABS, Lusófona University, 1749-024 Lisbon, Portugal (e-mail: brena.lima@ulusofona.pt).

João Pedro Matos-Carvalho is with the Center of Technology and Systems (CTS) and the Associated Laboratory of Intelligent Systems (LASI), UNINOVA, 2829-516 Caparica, Portugal, and also with COPELABS, Lusófona University, 1749-024 Lisbon, Portugal (e-mail: joao.matos.carvalho@ulusofona.pt).

Rui Dinis and Rodolfo Oliveira are with the Department of Electrical Engineering, NOVA University Lisbon, 1099-085 Caparica, Portugal, and also with the Instituto de Telecomunicações, 3810-193 Lisbon, Portugal (e-mail: rdinis@fct.unl.pt; rado@fct.unl.pt).

Daniel Benevides da Costa is with the Department of Electrical Engineering, Interdisciplinary Research Center for Communication Systems and Sensing, King Fahd University of Petroleum and Minerals (KFUPM), Dhahran 31261, Saudi Arabia (e-mail: danielbcosta@ieee.org).

Marko Beko is with the Instituto de Telecomunicações, Instituto Superior Técnico, University of Lisbon, 1649-004 Lisbon, Portugal, and also with COPELABS, Lusófona University, 1749-024 Lisbon, Portugal (e-mail: marko.beko@tecnico.ulisboa.pt).

Color versions of one or more figures in this article are available at https://doi.org/10.1109/TCOMM.2024.3407192.

Digital Object Identifier 10.1109/TCOMM.2024.3407192

I. Introduction

RATE-SPLITTING multiple access (RSMA) scheme has received considerable attention as a promising enabling technique in 6G networks due to the more general and robust transmission framework [1], [2]. In contrast with non-orthogonal multiple access (NOMA), where the messages are superposed into only one stream with different levels of power or spreading sequences [3], the message transmitted to the users in RSMA scheme is divided into a common message and private message by applying superposition coding at the base station (BS). Then, both common and private messages are simultaneously transmitted, in which the extra degrees of freedom (DoF) can be achieved by exploiting smartly the common message(s). At the receivers, the decoding process is carried out by using successive interference cancelation (SIC) techniques [4]. Specifically, the common message is decoded by all users and the private message is decoded only by the intended user. To decode the common message, the users first decode the interference part of the signal from other users. Assuming perfect SIC, the intended user decodes its private message, treating the private message of the remaining users as interference.

In order to customize the propagation environment of future communication systems, intelligent reflecting surfaces (IRSs) arise as a promising technology to assist RSMA networks. An IRS is a planar metasurface composed of a large number of reflecting elements that can be programmed independently to induce distinct phase and amplitude changes to reflect and steer impinging waves towards any desired direction [5]. Despite the potential gains, few works exploit the combination of IRS and RSMA [6], [7], [8], [9]. By exploring a terrestrial IRS (TIRS) RSMA, the works [10] and [11] presented solutions for digital precoder, the rate-splitting vector, the reflecting vector, and for optimal power allocation at each user, passive beamforming at the IRS under optimal decoding order of sub-messages, respectively.

By deploying IRS on aerial platforms, it is possible to achieve numerous benefits when compared to the TIRS deployment [12], [13]. In particular, [14] provides a comprehensive discussion about the interplay of aerial IRS in multiple-input multiple-output (MIMO) NOMA networks, as well as its architecture, functionality principles, and performance gains. For instance, aerial IRS (AIRS) can provide flexible deployment and full-angle panoramic reflection (360Â°) [15]. In [16], the authors formulated a robust secrecy rate maximization problem to enhance the security gain with aerial RIS reflection and jamming. In [17], the authors investigate the use of RSMA with finite blocklength codes in such networks and focus on joint optimization of 3D coordinates of the UAV/RIS and phase shift matrix at the RIS.

To face the highly dynamic environment and exploit the potential of IRSs in multiple access networks, solutions based on machine learning (ML) have been investigated over the years. In particular, the long short-term memory (LSTM) technique is a variant of recurrent neural network (RNN) and has been explored due to its potential to predict sequential patterns by recursively forwarding the previous information to the memory [18]. This fact, makes LSTM specialized in extracting resources from the dynamic environment.

A. Related Works

Research efforts have been carried out in the field of LSTM-enhanced wireless networks. The work [19] explored an LSTM-based algorithm in a NOMA network to detect the channel characteristics automatically. In [20] and [21], an LSTM was used to extract the sequential correlated features from the channel information to reduce the energy consumption of the network and to eliminate the need for the use of SIC for uplink and downlink for RSMA networks, respectively.

Related to the RIS/IRS field, the work [22] investigated an IRS-MISO NOMA. The authors adopted an LSTM-based algorithm for predicting the mobility of users, a K-means-based Gaussian model for user clustering, and a deep Q-network (DQN)-based algorithm for jointly determining the phase shift matrix and power allocation policy. In [23], the trajectories and NOMA decoding orders of robots, phase-shift of the RIS, and the power allocation of the AP were optimized via LSTM and dueling double deep Q-network (D3QN) algorithm. In [24], a deep learning (DL)-based channel estimation method using a convolutional LSTM model was proposed. The algorithm exploits the characteristics of spatial features and temporal features of a time-series dataset to predict channel features. The authors [25] explore satellite-aerial-ground networks and aerial RIS to reflect the uplink signals from the ground devices to high-altitude platforms. The system ergodic sum-rate is optimized by exploring LSTM-deep deterministic policy gradient (DDPG) algorithm. In [26], LSTM and convolutional neural networks were combined to predict the locations, line-of-sight (LoS), and no line-of-sight (NLoS) status of the users. In [27], an LSTM-based algorithm was proposed to perform decision-making by using data about channel state and RIS's energy harvesting. The LSTM uses the current configuration of the IRS, the BS's transmission power, and the receiver's location as input in the training phase. In [28], the authors proposed an LSTM-based algorithm to control the phase shift in the terrestrial RIS-aided systems. The algorithm exploits and learns temporal variation of channels from past pilot sequences.

By exploring UAV-enabled wireless networks, [29] proposed an algorithm based on Kalman filtering and LSTM to improve the beam tracking accuracy and spectrum efficiency, while reducing the overheads of high-speed railway wireless networks. The authors in [30] proposed a method by combining DDPG and LSTM to minimize the total energy consumption of the UAV and maximize the system throughput and the total harvested energy. In [31], the authors proposed an LSTM-based method to predict cellular traffic. The authors in [32] performed a data preprocessing of the spatio-temporal parameters such as longitude, latitude, altitude, and time. Then, an LSTM-based model is applied to predict the UAV's position. The works [33], [34] also explored problems related to the UAV trajectory, in which an LSTM-based layer was used to optimize trajectory and velocity by predicting the time-varying energy harvesting and channel conditions.

B. Motivation and Contributions

Although the aforementioned research contributions have provided solutions for AIRS or TIRS with different multiple access techniques, there is some published work that specifically investigates the integration of AIRS in RSMA networks. In particular, in [9], expressions for the approximate cumulative distribution function of common and private stream signal-to-interference-plus-noise ratios (SINR), and the average outage probability were derived. In addition, by using an iterative algorithm, the power allocation coefficients in each time slot of UAV flight duration are obtained. In a similar vein, the work [35] investigated a RIS-UAV-aided RSMA network. RSMA parameters, 3D-coordinates of the aerial RIS, and phase shift matrix at the RIS were jointly optimized by using a heuristic approach for optimum power allocation. In [36], a two-user scenario was explored and just beamforming was optimized. Although recent work has investigated AIRS-RSMA systems, the effects of the dynamic environment are still not clarified, and machine learning (ML)-based solutions such as the powerful LSTM technique have not been explored. In order to fill out this gap in the literature, this paper investigates downlink AIRS-aided multiple-input single-output (MISO) RSMA (AIRS-RSMA) networks, taking into account the effects of imperfect SIC in the environment. In contrast with [36], where a two-user scenario was explored and only beamforming was optimized, this work explores a multiuser scenario, for both static and dynamic user movement, in which beamforming at BS, the trajectory of the UAV, and the phase-shift of the AIRS were optimized by combining conventional optimization method and machine learning approaches. Further details and the main contributions of this work are summarized as follows:

- A beamforming design is proposed under the assumption of imperfect SIC for multiuser scenarios. In particular, an optimization problem is formulated in order to

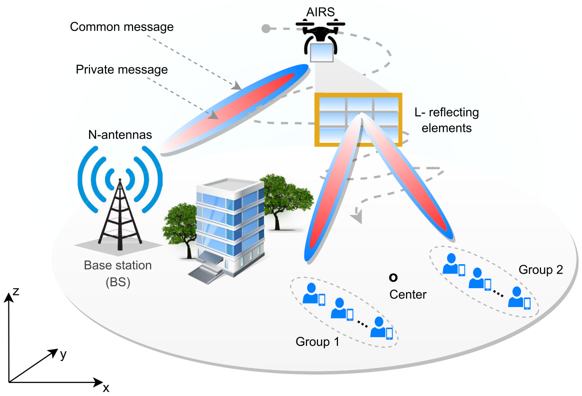

Fig. 1. Illustration of AIRS-RSMA network with two groups of users.

maximize the total achievable rate by optimizing the transmit beamforming at the BS and common rates to the users. The optimization problem is converted into a semi-definite program (SDP) problem and an alternating optimization (AO)-based method is used to design a suboptimal algorithm.

- LSTM-based algorithms are developed to accurately design the trajectory of the UAV and the phase-shift of the AIRS, taking into account the centroid of each user group. To improve the achievable rate of the system, two learning policies are proposed, in which the scenarios with static and dynamic users are explored. Then, two LSTM-based networks are employed to predict the next positions of the UAV and the efficient phase-shift of AIRS.
- The UAV is configured to follow a new trajectory, aiming to maximize the total achievable rate of the system, while the phase-shift is optimized to maximize the sum-rate of each group. At each time step t, the UAV assumes a new position, calculates the instantaneous sum-rate, and compares it with the sum-rate obtained at time $t-1$. If the sum-rate at time t, is lower than that at time $t-1$, the UAV reverts to its previous position and recalculates a new position to maximize the total achievable rate at time $t+1$.
- Training and test results are presented to demonstrate the potential of the proposed scheme, as well as numerical simulation results. The results show that the proposed models efficiently predict the UAV's trajectory and phase-shift vectors to maximize the sum-rate of the systems for static and dynamic scenarios.

II. System Model

Consider a MISO-RSMA downlink network where one base station (BS) equipped with N antennas communicates with G clusters composed of U single-antenna ground users. Users are clustered based on their channel gain and distance from each other [37]. To this end, the principles of K-means are exploited. For simplicity, we assume that each group consists of K users, i.e., $U = GK$. Due to the blockage, it is assumed that there is no direct link between the BS and the k-th user of the g-th cluster, in which $k \in \mathcal{K} = \{1, \cdots, K\}$ and $g \in \mathcal{G} = \{1, \cdots, G\}$. Thus, an IRS with L reflecting elements, denoted by $\mathcal{L} = \{1, \cdots, L\}$, is deployed at the UAV to enable communication between the BS and the users. In addition, it is assumed that the UAV continuously flies with a constant velocity in a 3D plane. Note that the beamforming at BS, the phase-shift matrix of AIRS, and the UAV trajectory will be explored in depth in the following sections. The proposed method is versatile and with great potential for adaptability, trained to enable and enhance communication in two scenarios. In the first scenario, it is assumed that the users are arranged in a static way, while in the second scenario, the users are in constant mobility in a delimited area.

Based on RSMA principles, the message intended for k-th user within g-th group is split into a common part, s^c_{gk}, and a private part, s^p_{gk}, [1]. Specifically, the messages of each user within each group are encoded together in a common stream $s^c_g = (s^c_{g1}, \cdots, s^c_{gK})$, using a codebook shared by the k-th user of the g-th group, while the private parts are encoded independently into private streams s^p_{gk}. At the transmitter, the data streams are linearly precoded and superimposed in the power domain, then simultaneously transmitted. As a result, the signal transmitted by the BS can be expressed as

$$\mathbf{x} = \sum_{g=1}^{G} \left(\mathbf{p}^c_g \sqrt{\alpha^c_g} s^c_g + \sum_{k=1}^{K} \mathbf{p}^p_{gk} \sqrt{\alpha^p_{gk}} s^p_{gk} \right) \in \mathbb{C}^{N \times 1}, \quad (1)$$

where the vector of symbol streams to be transmitted to the g-th group can be denoted by $\mathbf{s}_g = [s^c_g \alpha^c_g, s_{g1}\alpha^p_{g1}, \cdots, s_{gK}\alpha_{gK}]^T \in \mathbb{C}^{(K+1)\times 1}$, where α^c_g and α^p_{gk} are, respectively, the power allocation coefficients for the common and private messages in which $\alpha^c_g + \sum_{k=1}^{K} \alpha^p_{gk} = 1$, $\mathbf{p}^c_g \in \mathbb{C}^{N\times 1}$ denotes the beamforming vector of the common message serving all users within g-th group and $\mathbf{p}^p_{gk} \in \mathbb{C}^{N\times 1}$ represents the beamforming vector of the private message for the k-th user of the g-th group. For notation simplicity, the precoding vectors intended for the g-th group are reexpressed by $\mathbf{P}_g = [\mathbf{p}^c_g, \mathbf{p}^p_{g1}, \cdots, \mathbf{p}^p_{gK}] \in \mathbb{C}^{N\times(K+1)}$, where $\mathbf{P}_g$ stands for the beamforming matrix of the g-th user group.

The channel gain links between the BS and the AIRS, and the AIRS and the k-th user of the g-th group can be written, respectively, as

$$\ddot{\mathbf{H}} = \sqrt{\beta_l}\tilde{\mathbf{H}} \in \mathbb{C}^{N\times L}, \quad (2)$$

and

$$\ddot{\mathbf{h}}_{gk} = \sqrt{\beta_{gk}}\tilde{\mathbf{h}}_{gk} \in \mathbb{C}^{L\times 1}, \ \forall k \in \mathcal{K}, \forall g \in \mathcal{G}, \quad (3)$$

where $\tilde{\mathbf{H}}$ and $\tilde{\mathbf{h}}_{gk}$ denote the small-scale fading, modeled by the Nakagami distribution, as in [12]. The parameters $\beta_l = \beta_0 d_l^{-\nu}$ and $\beta_{gk} = d_{gk}^{-\nu}$ denote, respectively, the large-scale average channel power gain between the BS and the AIRS, and the AIRS and the k-th user of the g-th group, in which β_0 symbolizes the gain parameter. The parameters d_l and d_{gk} mean the distance between the BS and the AIRS, and the AIRS and the k-th user of the g-th group. In addition, ν refers to the pathloss exponent. Based on three-dimensional Cartesian coordinates, the location of the UAV can be represented by (x^t_l, y^t_l, z^t_l) and the location of the k-th user within the g-th group at the t time step by $(x_{gk}^t, y_{gk}^t, 0)$, the distances d_l and d_{gk} can be given, respectively, by

$$d_l^t = \sqrt{(x_0 - x_l^t)^2 + (y_0 - y_l^t)^2 + (z_l^t)^2}, \tag{4}$$

and

$$d_{gk}^t = \sqrt{(x_l^t - x_{gk}^t)^2 + (y_l^t - y_{gk}^t)^2 + (z_l^t)^2}. \tag{5}$$

For each time step t, the UAV chooses a new position to cross according to the centroid of each group. Since the users are in mobility, their distances are also recalculated in each time step. The data related to the distance will be deeply explored in the following sections, specifically in the trajectory training subsection.

It is assumed that the AIRS is equipped with a controller that can smartly adjust the AIRS's phase shifts. To characterize the phase shifts, in training step, it is considered that the phase-shift matrix of the AIRS is diagonal and can be written as [12] $\mathbf{\Phi} = \text{diag}[\kappa_1 e^{j\theta_1}, \kappa_2 e^{j\theta_2}, \ldots, \kappa_L e^{j\theta_L}] \in \mathbb{C}^{L\times L}$, denotes the phase-shift occurring at r-th element of the AIRS, in which $|\kappa_l e^{j\theta_l}| = 1$ for $\theta_l \in [0, 2\pi)$ and $l \in \mathcal{L}$, and κ_l refers to the fixed amplitude reflection coefficient. We assume that $\kappa_l = 1$, as commonly adopted in the literature, i.e., [22], [23]. For practical implementation purposes, we consider that discrete phase shifts are adopted at each element of the AIRS. Then, each element of the AIRS can take a finite number of values by uniformly quantizing the interval $[0, 2\pi)$, which can be expressed as [38]

$$\theta_l \in \left\{\frac{2\pi n}{2^{\ddot{b}}}, n = 0, 1, 2, \cdots, 2^{\ddot{b}} - 1\right\}, \quad \forall l \in \mathcal{L}. \tag{6}$$

where $\ddot{b}$ denotes the bit resolution. The interval in (6) is used in the training process of our proposed DL models.

In particular, the effective end-to-end (e2e) channel gain from the BS to k-th user of the g-th group via AIRS is given by

$$\mathbf{h}_{gk} = \ddot{\mathbf{h}}_{gk}^H \mathbf{\Phi} \ddot{\mathbf{H}} \in \mathbb{C}^{N\times 1}. \tag{7}$$

The signal received at the k-th user of the g-th group can be expressed as $y_{gk} = \mathbf{h}_{gk}\mathbf{x} + \omega_{gk}$, where $\omega_{gk} \sim \mathcal{CN}(0, \sigma^2)$ denotes the additive white Gaussian noise (AWGN) at the k-th user within g-th group.

In RSMA systems, the SIC technique is used once in each receiver to separate the common and private messages. After the common message is separated using SIC, the private message of a specific user can be decoded, considering the private message of the other users as interference. Specifically, the corresponding signal-to-interference-plus-noise ratio (SINR) to decode the common message at the k-th user of the g-th group is given by

$$\gamma_{gk}^c = \frac{\rho|\mathbf{h}_{gk}\mathbf{p}_g^c|^2\alpha_g^c}{\rho\sum_{i=1}^K |\mathbf{h}_{gk}\mathbf{p}_{gi}^p|^2\alpha_{gi}^p + 1}, \tag{8}$$

where ρ means the transmit signal-to-noise ratio (SNR). By considering imperfect SIC, the k-th user of the g-th group must decode its private message taking into account the other users' private messages and the common message as noise. Thus, the SINR to decode the private message at the k-th user of the g-th group is given by

$$\gamma_{gk}^p = \frac{\rho|\mathbf{h}_{gk}\mathbf{p}_{gk}^p|^2\alpha_{gk}^p}{\rho|\mathbf{h}_{gk}\mathbf{p}_g^c|^2\alpha_g^c\epsilon + \rho\sum_{i\neq k}^K |\mathbf{h}_{gk}\mathbf{p}_{gi}^p|^2\alpha_{gi}^p + 1}, \tag{9}$$

where $\epsilon \in [0, 1]$ is the coefficient of imperfect SIC. On one hand, the instantaneous achievable rate of the k-th user of the g-th group in decoding the common message can be expressed as

$$r_{gk}^c = \log_2(1 + \gamma_{gk}^c). \tag{10}$$

On the other hand, the e2e instantaneous achievable rate of the k-th user in decoding its desired private message can be expressed as

$$r_{gk}^p = \log_2(1 + \gamma_{gk}^p). \tag{11}$$

Since the common message is shared amongst all users, the rate of the common message is formulated as $\bar{r}_{gi}^c = \min_{k\in\mathcal{K}}\{r_{gk}^c\}$ to ensure that all users can decode the common message. Given the common rate $\bar{r}_{gk}^c$, the constraint $\sum_{i=1}^K \alpha_g^c \leq \bar{r}_{gi}^c$ should be satisfied.

Finally, based on the achievable common rate $\bar{r}_{gk}^c$ and achievable private rate r_{gk}^p, the total achievable rate of the k-th user can be expressed as

$$R_{gk}^{\text{tot}} = \bar{r}_{gk}^c + r_{gk}^p. \tag{12}$$

Next, it is formulated a beamforming design for the proposed AIRS-RSMA network.

III. Beamforming Design

Given the considered system model, we formulate an optimization problem to maximize the minimum total achieved rate via transmit beamforming optimization at BS and achievable common rate at the users, taking into account imperfect SIC. The optimization problem can be formulated as

$$\max_{\mathbf{P}_g, \bar{\mathbf{r}}_g^c} \min_{k\in K}\{R_{gk}^{\text{tot}}\}, \tag{13a}$$

$$\text{subject to } C1: \ r_{gk}^c \geq \sum_{i=1}^K \bar{r}_{gi}^c, \forall k \in \mathcal{K}, \forall g \in \mathcal{G}, \tag{13b}$$

$$C2: ||\mathbf{p}_g^c||^2 + \sum_{i=1}^K ||\mathbf{p}_{gi}^p||^2 \leq P_{tot}, \tag{13c}$$

$$C3: \ \bar{\mathbf{r}}_g^c \geq 0, \tag{13d}$$

$$C4: \ \alpha_{gk}^c + \sum_{i=1}^K \alpha_{gi}^p = 1, \tag{13e}$$

where $\bar{\mathbf{r}}_g^c = [\bar{r}_{g1}^c, \cdots, \bar{r}_{gK}^c]^T$ denotes the vector of achievable common rate among users within g-th group, which is optimized together with the precoding matrix $\mathbf{P}_g$, and P_{tot} refers to the maximum transmit power at BS. Constraint (13b) ensures that all users can decode correctly the common message. Constraint (13d) is imposed to guarantee that the common rate achieved by k-th user of the g-th group is non-negative.

To solve the problem (13a), we first transform it into its epigraph form to facilitate the design of a method based on majorization minimization. Firstly, we introduce two optimization variables, $\mathbf{r}_g^p = [r_{g1}^p, \cdots, r_{gK}^p]^T \geq 0$ and $\Omega_g \geq 0$. The problem (13a) can be rewritten as

$$\max_{\mathbf{P}_g, \bar{\mathbf{r}}_g^c, \mathbf{r}_g^p, \Omega_g} \Omega_g, \tag{14a}$$

$$\text{subject to } C1: \; R_{gk}^{\text{tot}} \geq \Omega_g, \tag{14b}$$

$$C2: A_{gk}^c(\mathbf{P}_g) + B_{gk}^c(\mathbf{P}_g) \geq \sum_{i=1}^{K} \bar{r}_{gi}^c, \tag{14c}$$

$$C3: C_{gk}^p(\mathbf{P}_g) + D_{gk}^p(\mathbf{P}_g) \geq r_{gk}^p, \tag{14d}$$

$$C4: \text{Tr}\left(\mathbf{p}_g^c + \sum_{i=1}^{K} \mathbf{p}_{gi}^p\right) \leq P_{tot}, \tag{14e}$$

$$C5: \; \bar{r}_{gk}^c \geq 0 \text{ and } r_{gk}^p \geq 0, \tag{14f}$$

$$C6: \; \mathbf{P}_g \succeq 0, \tag{14g}$$

$$C7: \; \text{Rank}(\mathbf{P}_g) = 1, \tag{14h}$$

where

$$A_{gk}^c(\mathbf{P}_g) = \log_2\Bigg(\rho \mathbf{h}_{gk} \mathbf{P}_g^c \mathbf{h}_{gk}^H \alpha_g^c + \rho \sum_{i=1}^{K} \mathbf{h}_{gk} \mathbf{P}_i^p \mathbf{h}_{gk}^H \alpha_{gi}^p + 1\Bigg), \forall k, \forall g, \tag{15}$$

$$B_{gk}^c(\mathbf{P}_g) = -\log_2\left(\rho \sum_{i=1}^{K} \mathbf{h}_{gk} \mathbf{P}_{gi}^p \mathbf{h}_{gk}^H \alpha_{gi}^p + 1\right), \forall k, \forall g, \tag{16}$$

$$C_{gk}^p(\mathbf{P}_g) = \log_2\Bigg(\rho \mathbf{h}_{gk} \mathbf{P}_g^c \mathbf{h}_k^H \alpha_g^c \epsilon + \rho \sum_{i \neq k}^{K} \mathbf{h}_{gk} \mathbf{P}_{gi}^p \mathbf{h}_{gk}^H \alpha_{gi}^p + \rho \sum_{i=1}^{K} \mathbf{h}_{gk} \mathbf{P}_{gi}^p \mathbf{h}_{gk}^H \alpha_{gi}^p + 1\Bigg), \forall k, \forall g, \tag{17}$$

$$D_{gk}^p(\mathbf{P}_g) = -\log_2\Bigg(\rho \mathbf{h}_{gk} \mathbf{P}_g^c \mathbf{h}_{gk}^H \alpha_g^c \epsilon + \rho \sum_{i \neq k}^{K} \mathbf{h}_{gk} \mathbf{P}_{gi}^p \mathbf{h}_{gk}^H \alpha_{gi}^p + 1\Bigg), \forall k, \forall g, \tag{18}$$

where $\mathbf{P}_g^c = \mathbf{p}_g^c \mathbf{p}_g^{cH}$ and $\mathbf{P}_{gk}^p = \mathbf{p}_{gk}^p \mathbf{p}_{gk}^{pH}$, with $g \in \mathcal{G}$ and $k \in \mathcal{K}$, Ω_g is an auxiliary optimization variable, $\text{Tr}(\cdot)$ denotes the trace of a matrix, and $\text{Rank}(\cdot)$ means the rank of the matrix. Since the elements of constraints (14c) and (14d) are concave, specifically (15) and (17), while (16) and (18) are non-convex, the problem (14a) is non-convex. However, these constraints are expressed in the form of difference of convex functions. Thus, (14c) and (14d) can be rewritten by their corresponding lower bound functions to tackle the non-convex parts. In addition, constraints (14g) and (14h) are imposed to guarantee that $\mathbf{P}_g$ holds after optimization, in which the rank-one constraint in (14h) can be tackled by applying semi-definite relaxation technique. In particular, for handling the non-convex parts of constraints (14c) and (14d), we use the following proposition.

Proposition 1 [39]: Let $a \in \mathbb{R}^{1\times 1}$ be a positive scalar and $f(a) = -(ab/\ln 2) + \log_2 a + (1/\ln 2)$. It follows that

$$-\log_2 b = \max_{a>0} f(a), \tag{19}$$

and the optimal solution to the right-hand side of (19) is $a = 1/b$.

Proof: Since $f(a)$ is concave, the optimal solution to the right-hand side of (19) is obtained by setting $\partial f(a)/\partial a = 0$. ■

By applying Proposition 1 in (14a), we transform the elements (16) and (18) into convex optimization problems. In the t-th iteration, we approximate $B_{gk}^c(\mathbf{P}_g)$ and $D_{gk}^p(\mathbf{P}_g)$ as affine functions by using their corresponding lower bound functions. Thus, we have the following problems

$$B_{gk}^c(\mathbf{P}_g) \geq \max_{\varrho_{gk}^c \in \mathbb{R}^{1\times 1},\, \varrho_{gk}^c > 0} \xi_{gk}^c(\varrho_{gk}^c), \forall k \in \mathcal{K}, \forall g \in \mathcal{G}, \tag{20}$$

$$D_{gk}^p(\mathbf{P}_g) \geq \max_{\varrho_{gk}^p \in \mathbb{R}^{1\times 1},\, \varrho_{gk}^p > 0} \xi_{gk}^p(\varrho_{gk}^p), \forall k \in \mathcal{K}, \forall g \in \mathcal{G}, \tag{21}$$

where

$$\xi_{gk}^c(\varrho_{gk}^c) = -\frac{\varrho_{gk}^c}{\ln 2}\left(\rho \sum_{i=1}^{K} \mathbf{h}_{gk} \mathbf{P}_{gi}^p \mathbf{h}_{gk}^H \alpha_{gi}^p + 1\right) + \log_2(\varrho_{gk}^c) + \frac{1}{\ln 2}, \tag{22}$$

and

$$\xi_{gk}^p(\varrho_{gk}^p) = -\frac{\varrho_{gk}^p}{\ln 2}\Bigg(\rho \mathbf{h}_{gk} \mathbf{P}_g^c \mathbf{h}_{gk}^H \alpha_g^c \epsilon + \rho \sum_{i \neq k}^{K} \mathbf{h}_{gk} \mathbf{P}_{gi}^p \mathbf{h}_{gk}^H \alpha_{gi}^p + 1\Bigg) + \log_2(\varrho_{gk}^p) + \frac{1}{\ln 2}. \tag{23}$$

According to Proposition 1, when the optimal $\mathbf{P}_g^{(t)}$ in the $(t-1)$-th iteration, which is denoted by $\mathbf{P}_g^{(t-1)}$, is obtained, ϱ_{gk}^c and ϱ_{gk}^p can be updated in the t-th iteration by solving

$${\varrho_{gk}^c}^{(t)} = \arg\max_{\varrho_{gk}^c > 0} -\frac{\varrho_{gk}^c}{\ln 2}\left(\rho \sum_{i=1}^{K} \mathbf{h}_{gk} {\mathbf{P}_{gi}^p}^{(t-1)} \mathbf{h}_{gk}^H \alpha_{gi}^p + 1\right) + \log_2(\varrho_{gk}^c) + \frac{1}{\ln 2}, \forall k \in \mathcal{K}, \forall g \in \mathcal{G}, \tag{24}$$

and

$${\varrho_{gk}^p}^{(t)} = \arg\max_{\varrho_{gk}^p > 0} -\frac{\varrho_{gk}^p}{\ln 2}\Bigg(\rho \mathbf{h}_{gk} {\mathbf{P}_g^c}^{(t-1)} \mathbf{h}_{gk}^H \alpha_g^c \epsilon + \rho \sum_{i \neq k}^{K} \mathbf{h}_{gk} {\mathbf{P}_{gi}^p}^{(t-1)} \mathbf{h}_{gk}^H \alpha_{gi}^p + 1\Bigg) + \log_2(\varrho_{gk}^p) + \frac{1}{\ln 2}, \forall k \in \mathcal{K}, \forall g \in \mathcal{G}. \tag{25}$$

Since it is assumed perfect CSI at the BS, (24) and (25) can be rewritten, respectively, as [39]

$${\varrho_{gk}^c}^{(t)} = \left(\rho \sum_{i=1}^{K} \mathbf{h}_{gk} {\mathbf{P}_{gi}^p}^{(t-1)} \mathbf{h}_{gk}^H \alpha_{gi}^p + 1\right)^{-1}, \tag{26}$$

and

$${\varrho_{gk}^p}^{(t)} = \Bigg(\rho \mathbf{h}_{gk} {\mathbf{P}_g^c}^{(t-1)} \mathbf{h}_{gk}^H \alpha_g^c \epsilon + \rho \sum_{i \neq k}^{K} \mathbf{h}_{gk} {\mathbf{P}_{gi}^p}^{(t-1)} \mathbf{h}_{gk}^H \alpha_{gi}^p + 1\Bigg)^{-1}. \tag{27}$$

Based on the solution ${\mathbf{P}_g}^{(t-1)}$ obtained in the $(t-1)$-th iteration, the global underestimation of $B^c_{gk}(\mathbf{P}_g)$ in (16) can be iteratively approximated at the t-th iteration. Then, $B^c_{gk}(\mathbf{P}_g)$ can be re-expressed based on its lower bound function, given by $\ddot{B}^c_{gk}({\mathbf{P}_g}^{(t-1)})$ in (28), as shown at the bottom of the page.

In a parallel avenue, in t-th iteration $D^p_{gk}(\mathbf{P}_g)$ in (18) is replaced by its lower bound. Its corresponding lower bound solution is given by $\ddot{D}^p_{gk}({\mathbf{P}_g}^{(t-1)})$, shown in (29), as shown at the bottom of the page.

As a result, the problem (14a) can be expressed based on its lower bound functions and, therefore, reformulated as follows

$$\max_{\mathbf{P}_g^{(t)},\bar{\mathbf{r}}_g^c,\mathbf{r}_g^p,\Omega_g} \quad \Omega_g, \tag{30a}$$

$$\text{subject to } C1: \; R^{\text{tot}}_{gk} \geq \Omega_g, \tag{30b}$$

$$C2: \; A^c_{gk}(\mathbf{P}^{c\,(t)}_g) + \ddot{B}^c_{gk}(\mathbf{P}^{c\,(t-1)}_g) \geq \sum_{i=1}^{K} \bar{r}^c_{gi}, \tag{30c}$$

$$C3: \; C^p_{gk}({\mathbf{P}^p_{gk}}^{(t)}) + \ddot{D}^p_{gk}({\mathbf{P}^p_{gk}}^{(t-1)}) \geq r^p_{gk}, \tag{30d}$$

$$C4: \; \text{Tr}(\mathbf{P}^c_g + \sum_{k=1}^{K} \mathbf{P}^p_{gk}) \leq P_{tot}, \tag{30e}$$

$$C5: \; \bar{r}^c_{gk} \geq 0 \text{ and } r^p_{gk} \geq 0, \tag{30f}$$

$$C6: \; \mathbf{P}_g \succeq 0, \tag{30g}$$

$$C7: \; \text{Rank}(\mathbf{P}^c_g) = 1, \; \text{Rank}(\mathbf{P}^p_{gk}) = 1. \tag{30h}$$

One can notice that the problem (30a) consists of an SDP problem. Thus, one can use the AO approach to design a suboptimal iterative algorithm in order to optimize $\varrho^{c(t)}_{gk}$, $\varrho^{p(t)}_{gk}$, and $\mathbf{P}_g$, $\forall k \in \mathcal{K}$, and $\forall g \in \mathcal{G}$, at each iteration. If the optimal matrix solutions to the problem (30a) are rank one, then the optimal precoders are defined as the optimal solution to the problem. To verify that the relaxed problem satisfies the rank-one condition, the following proposition is presented.

Proposition 2: The solution $\mathbf{P}^*_g$ of the problem (30a) satisfies the rank-one conditions.

Proof: Please refer to Appendix.

Thus, by performing an eigenvalue decomposition on the solution $\mathbf{P}^*_g$, the beamforming vector that maximizes the achievable rate is obtained by selecting the principal eigenvector. The proposed algorithm to realize the above alternating optimization is summarized in Algorithm 1. Since $\mathbf{P}_g$ and $\bar{\mathbf{r}}^c_g$ are optimized, the objective value is non-decreasing and the convergence of problem (30a) is guaranteed for a sufficient number of iterations $T_{\max}$. On the other hand, the stop criteria $|\Omega^{(t)}_g - {\Omega_g}^{(t-1)}| < \tau$ controls the convergence of Algorithm 1.

Algorithm 1 AO Algorithm for Beamforming Design in AIRS-RSMA Networks

1. **Initialize:** $\mathbf{P}^{(0)}_g$ $\forall g \in \mathcal{G}$, set the convergence index $\tau = 10^{-4}$, and the number of iteration $t = 1$;
4. **Repeat:**
   1. In the t-th iteration, approximate $B^c_{gk}(\mathbf{P}_g)$ and $D^p_{gk}(\mathbf{P}_g)$ as affine functions by using their corresponding lower bound functions obtained by solving (20) and (21).
   2. Solve (26) and (27) to obtain $\varrho^{c(t)}_{gk}$ and $\varrho^{p(t)}_{pk}$, respectively;
   3. With the given $\varrho^{c(t)}_{gk}$ and $\varrho^{p(t)}_{gk}$, solve the problem (30a) to obtain $\mathbf{P}^{(t)}_g$;
   5. Given $\mathbf{P}^{(t)}_g$, solve (10) and (11) to obtain $\bar{r}^c_{gk}$, and r^p_{gk};
   6. Update iteration $t = t + 1$;
5. **Until:** $|\Omega^{(t)}_g - {\Omega_g}^{(t-1)}| < \tau$ or $t = T_{\max}$;
6. **Output:** $\mathbf{P}^*_g = [\mathbf{P}^{c*}_g, \mathbf{P}^{p*}_{gk}]$, $\bar{r}^c_{gk}$, and r^p_{gk}, $\forall k \in \mathcal{K}$ and $\forall g \in \mathcal{G}$.

Remark: The complexity of solving an SDP problem is $\mathcal{O}(n^{1/2}_{\text{sdp}} \cdot (m_{\text{sdp}} n^3_{\text{sdp}} + m^2_{\text{sdp}} n^2_{\text{sdp}} + m^3_{\text{sdp}})) \cdot \log(1/\tau)$ [40], where m_{sdp} is the number of semidefinite cone constraints, n_{sdp} represents the dimension of the semidefinite cone, and τ denotes the accuracy of solving the problem. Since we have T number of alternating optimization, $m_{\text{sdp}} = 7$ and $n_{\text{sdp}} = (N+1)$, the computational complexity of the problem can be expressed as

$$T \cdot \mathcal{O}(7(N+1)^{\frac{7}{2}} + 49(N+1)^{\frac{5}{2}} + 343(N+1)^{\frac{1}{2}}) \cdot \log(\frac{1}{\tau}). \tag{31}$$

IV. Phase-Shift and Trajectory Optimization With LSTM

A. Long Short-Term Memory Networks

LSTM are part of a group of architectures called RNN, which are a family of neural networks widely used for models whose problems are characterized by data sequences [41], [42], [43]. These two types of networks differ from other neural networks since the network parameters are shared along

$$\ddot{B}^c_{gk}({\mathbf{P}_g}^{(t-1)}) = \max_{{\varrho^c_{pk}}^{(t)}>0} \; -\frac{{\varrho^c_{gk}}^{(t)}\left(\rho \sum_{i=1}^{K} \mathbf{h}_{gk} {\mathbf{P}^p_{gi}}^{(t)} \mathbf{h}^H_{gk} \alpha^p_{gi} + 1\right)}{\ln 2} + \log_2({\varrho^c_{gk}}^{(t)}) + \frac{1}{\ln 2}, \forall k \in \mathcal{K}, \tag{28}$$

$$\ddot{D}^p_{gk}({\mathbf{P}_g}^{(t-1)}) = \max_{{\varrho^p_{gk}}^{(t)}>0} \; -\frac{{\varrho^p_{gk}}^{(t)}\left(\rho \mathbf{h}_{gk} \mathbf{P}^{c\,(t)}_g \mathbf{h}^H_{gk} \alpha^c_g \epsilon + \rho \sum_{i \neq k}^{K} \mathbf{h}_{gk} {\mathbf{P}^p_{gi}}^{(t)} \mathbf{h}^H_{gk} \alpha^p_{gi} + 1\right)}{\ln 2} + \log_2({\varrho^p_{gk}}^{(t)}) + \frac{1}{\ln 2}, \forall k \in \mathcal{K}, \tag{29}$$

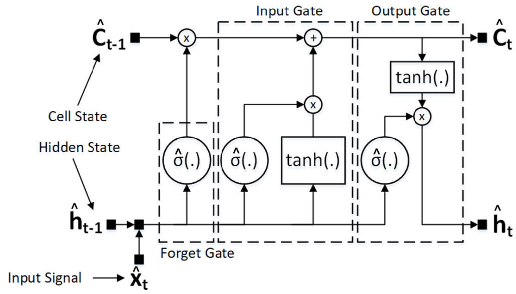

Fig. 2. Internal structure of the LSTM cell.

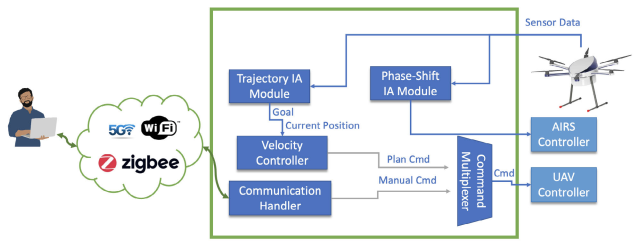

Fig. 3. Architecture of the proposed system.

several points of the sequence under analysis. The outputs of the previous elements influence each one of the output elements. This particularity of persistence of the characteristics present in the data allows the model to look at a sequence as a whole and not just at an individual element. Unlike other networks, RNNs use feedback from activation's from previous time slots as input from the network to make a decision for the current input. It should be noted that the sequences that the RNN analyzes correspond to a time interval δ, which may not refer precisely to the phenomenon of time duration in the real world.

Given the example of an LSTM cell and the complete internal structure illustrated in Fig. 2, where the input gate, the output, and the forget gate are represented by $\hat{\boldsymbol{i}}^{(t)}$, $\hat{\boldsymbol{o}}^{(t)}$ and $\hat{\boldsymbol{f}}^{(t)}$ respectively, and $\hat{\boldsymbol{x}}$, $\hat{\boldsymbol{C}}$ and $\hat{\boldsymbol{h}}$, correspond to the input, state and output of the current cell and the previous cell, that is, the time stamp $t-1$. The variable $\tilde{\boldsymbol{C}}^{(t)}$) represents the vector of new values that can be added to the state $\hat{\boldsymbol{C}}$. Then the final state $\hat{\boldsymbol{C}}$ of the previous LSTM cell may or may not be affected by the output of each of the three gates, creating a new state of the current cell.

B. Trajectory

The observation space used to train the network is composed of the location of the UAV and the sum-rate experienced by each group at the t-th interval of time. Since the training process is performed by considering two groups, the observation space for trajectory optimization can be expressed as

$$S^{\dagger} = \left[x_l^t, y_l^t, z_l^t, \sum_{k=1}^{K} R_{1k}^{\text{tot,t}}, \sum_{k=1}^{K} R_{2k}^{\text{tot,t}} \right]. \tag{32}$$

As shown in Fig. 3 the $S^{\dagger}$ is represented by the sensor data where there is a GPS, an AIRS and also an IMU. The information from these sensors will feed two AI modules, the module for trajectory prediction and the module for phase-shift prediction (the second module will be explained in Section IV-C). As for the trajectory AI module, it receives the UAV's current position and the rate of each user group and returns the next UAV position to be reached. To generate the UAV's next position, the parameters that were used to train the network are shown in Table I and Algorithm 2, where N_n denotes the amount of neurons in each layer, the input is equal to 5 which represents the current 3D UAV position (x, y and z) and the sum-rate experienced by each group. The model was implemented using Matlab with Deep Learning Tool Box associated. The model was also trained on a laptop with NVIDIA GeForce GTX 1060, 16GB RAM and Intel Core i7-8750H CPU @ 2.20GHz x 12.

TABLE I
THE PROPOSED CUSTOM RNN ARCHITECTURE HYPERPARAMETERS FOR AI TRAJECTORY MODEL

Layer	Output	Hyperparameters
INPUT	5x1	
LSTM_1	600	$N_n = 1440000$;
FC OUTPUT	3	$N_n = 1803$; optm=ADAM loss=Mean Square Error

Algorithm 2 The Proposed Training Model Phase of Section IV-B

Require: $\boldsymbol{e} = 1, \ldots, N$, $\boldsymbol{LSTM_1} = 600$,

```
// Build the Deep Learning Model
for e = 1,...,N do
    model[0] ← input
    model[1] ← LSTM_1
    model[2] ← FNN
    //Compile Model
    model ← Loss = Mean Square Error
    model ← Optimizer = Adam
    //Train Model
    model ← Dataset
    //Score model evaluation and save it
    results ← model.save
end for=0
```

When this position is generated by the trajectory AI module, this result will feed the drone's velocity controller so that it can adapt its current speed until it reaches the desired destination. This controller extends a proportional–integral–derivative (PID) controllers, where the variables change depending on the type of UAV, the UAV's velocity calculation on the three axes were based on [44], where:

$$\boldsymbol{e}\hat{\boldsymbol{P}}^{(t)} = \boldsymbol{g}\hat{\boldsymbol{P}}^{(t)} - \boldsymbol{c}\hat{\boldsymbol{P}}^{(t)}, \tag{33}$$

and

$$\boldsymbol{e}\hat{\boldsymbol{D}}^{(t)} = ||(\boldsymbol{e}\hat{\boldsymbol{Q}}^{(t)})||, \tag{34}$$

where $\boldsymbol{e}\hat{\boldsymbol{Q}}^{(t)}$ represents the error position, $\boldsymbol{g}\hat{\boldsymbol{Q}}^{(t)}$ the goal position, $\boldsymbol{c}\hat{\boldsymbol{Q}}^{(t)}$ the current position at time instant t, and $\boldsymbol{e}\hat{\boldsymbol{D}}^{(t)}$ is the distance error position $\boldsymbol{e}\hat{\boldsymbol{Q}}^{(t)}$.

With (33) and (34) it is possible to normalize the error as follows

$$\boldsymbol{e\hat{N}}^{(t)} = \frac{\boldsymbol{e\hat{P}}^{(t)}}{\boldsymbol{e\hat{D}}^{(t)}}, \tag{35}$$

where $\boldsymbol{e\hat{N}}^{(t)}$ is the error normalized. If the distance is lower than a certain threshold, τ (in this work, the threshold value is set to $\tau = 5$ meters, obtained by calculating the Euclidean distance for the coordinated x and y), (36) is activated.

$$\boldsymbol{v\hat{Q}}^{(t)} = \boldsymbol{e\hat{Q}}^{(t)} \cdot \left(\frac{\boldsymbol{e\hat{D}}^{(t)}}{\tau} \right)^{\hat{SF}}, \tag{36}$$

where $\boldsymbol{v\hat{Q}}^{(t)}$ is the velocity vector and $\hat{SF}$ is the Smooth Factor (the $\hat{SF}$ was set to 2 [44]). If the distance is higher than 5 meters (threshold), (37) is then used.

$$\boldsymbol{v\hat{Q}}^{(t)} = \boldsymbol{e\hat{N}}^{(t)} \cdot P\hat{M}V. \tag{37}$$

In (37), $P\hat{M}V = 2$ denotes the Param Max Velocity.

In this way, it is allowed to dynamically vary the UAV speed depending on the UAV distance in relation to the desired destination without any sudden changes regarding the UAV's acceleration.

The Command Multiplexer module subscribes to the manual topic controlled by a human and the trajectory AI module and prioritizes the manual topic in order to increase the safety of the UAV's navigation.

C. Phase-Shift

While the AI module in section IV-B predicts the next UAV position, this section will describe how the phase-shift for each user group is optimized. In particular, the observation space used as input to train the LSTM consists of UAV position, a phase vector, and the data related to the centroid of each group. In the training process, the phase-shift of the l-th element of the AIRS is chosen from an action set. Specifically, a set of actions is created, which is composed of different phase vectors of size L resulting from the permutation of possible values in (6). Then, at each instant of time t, the system takes an action from the action set. In the end, for each group of users, the action that maximizes the sum-rate is chosen. Therefore, we obtain the phase change that maximizes the rate of each group for a specific UAV position. This phase vector, also called action set, is used as input to the LSTM, as well as the UAV position and the coordinates of the centroid of the g-th group. Then, the observation space for phase shift optimization can be expressed as

$$S^{\ddagger} = \left[x_l^t, y_l^t, z_l^t, x_g^c, y_g^c, \theta_{g1}^* \cdots \theta_{gL}^* \right]. \tag{38}$$

where x_g^c and y_g^c denote the coordinates x and y of the centroid of the g-th group and θ_{gl}^* denotes the phase of the l-th element of the AIRS.

To generate the AIRS's next phase-shift, the parameters that were used to train the network are shown in Table II and Algorithm 3, where the input is the current phase-shift, the current UAV 3D position and the coordinates x_g^c and y_g^c of te centroid of the g-th group (65 values), the output is the next predicted phase-shift and N_n denotes the amount of neurons in each layer.

TABLE II
THE PROPOSED CUSTOM RNN ARCHITECTURE HYPERPARAMETERS FOR AI PHASE-SHIFT MODEL

Layer	Output	Hyperparameters
INPUT	65x1	
LSTM_1	600	$N_n = 1598400$;
LSTM_2	600	$N_n = 2882400$;
FC OUTPUT	60	$N_n = 36060$; optm=ADAM loss=Mean Square Error

Algorithm 3 The Proposed Training Model Phase of Section IV-C

Require: $\boldsymbol{e} = 1, \ldots, N$, $\boldsymbol{LSTM_1} = 600$, $\boldsymbol{LSTM_2} = 600$,
`//Build the Deep Learning Model`
for $\boldsymbol{e} = 1, \ldots, N$ **do**
  $\boldsymbol{model}[0] \leftarrow \boldsymbol{input}$
  $\boldsymbol{model}[1] \leftarrow \boldsymbol{LSTM}_1$
  $\boldsymbol{model}[2] \leftarrow \boldsymbol{LSTM}_2$
  $\boldsymbol{model}[3] \leftarrow \boldsymbol{FNN}$
  `//Compile Model`
  $model \leftarrow$ Loss = Mean Square Error
  $model \leftarrow$ Optimizer = Adam
  `//Train Model`
  $model \leftarrow$ Dataset
  `//Score model evaluation and save it`
  $results \leftarrow model.save$
end for=0

While in Section IV-B only one LSTM layer was used to build the model, in this section, as the network input is larger, it is necessary to increase the size of the network's LSTM layer. As mentioned in [41], it's better to split the LSTM layer into more than one to improve performance and reduce the complexity of the network, making the model more tiny, rather than increasing the size of just one LSTM layer. Another advantage of making the model more tiny is the ability to run these algorithms directly on the UAV, making the response action faster than sending and receiving the information via the cloud [45], [46].

V. RESULTS

In this section, simulation results are provided to evaluate the performance of the proposed method. It is considered a scenario with $N = 4$ antennas at the BS and $K = 3$ single-antenna users per group, which are positioned in a cell of radius of 200 m. The UAV continuously flies, following the height range $20 \leq z \leq 60$ in meters, and an IRS with $L = 60$ reflective elements is fitted to the UAV. In particular, it is assumed $\ddot{b} = 2$, $\nu = 2.2$, $\alpha_g^c = 0.9$, $\alpha_{gk}^p = 0.05$ $\forall k \in \mathcal{K}$, $\tau = 10^{-3}$, $T_{\max} = 10^3$, and $\beta_0 = 1000$. The parameter β_0 is adjusted based on the desired performance of the receivers [47]. For AIRS-NOMA scenario, it is considered $\alpha_{g1} = 0.7$, $\alpha_{g2} = 0.2$, and $\alpha_{g3} = 0.1$. When not specified,

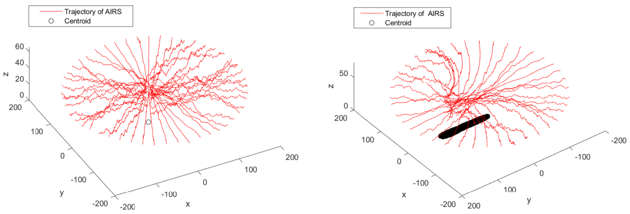

(a) Static scenario. (b) Dynamic scenario.

Fig. 4. Generating the observation space.

the value for SNR is set as 40 dB. In addition, it is assumed that the power consumption of IRS is 3 mW per element.

A. Training Progress

One of the crucial phases in the development of this system is the training phase for the models proposed in Sections IV-B and IV-C. By exploring the static scenario, Fig. 4a depicts the AIRS's trajectory in the training process based on the learning policy to find the centroid of the static user groups, as described in Section IV. In this figure, one can see that the UAV explores 50 starting points. The AIRS starts from one of these points and, at each time t, recalculates the distance to the center of the user groups based on linear equation. The coefficients of the equation of line are updated at each time t. Then, an observation space is generated by considering the data obtained for each starting point, as expressed in equations (32) and (38).

Similarly, Fig. 4b shows the training process, but now exploring the dynamic scenario. The learning policy is formulated by considering that the users are in movement, and a new observation space is generated. The observation spaces are used as input to the LSTM networks to predict the trajectory and phase-shift. In addition to the static and dynamic user group data that feeds the LSTM individually, further training was carried out in which this data (static and dynamic) is grouped together and fed into another LSTM network to also evaluate this information.

As the model for predicting the phase-shift is more complex than the model for predicting the trajectory (trajectory network returns 3 output values, while the phase-shift network returns a vector of size L, where $L > 3$), the number of epochs of the phase-shift will have to be higher in order to have an algorithm that can learn and predict with good performance. Thus, the model in Section IV-B has a number of epochs equal to 200, while the model in section IV-C was set to 500 epochs. The results can be observed in Figs. 5 and 6.

As can be seen in Figs. 5 and 6, the model that predicts the trajectory manages to converge more quickly than the model that predicts the phase-shift. This is due to the complexity of the network's input values, where the first model only needs five variables, and the second needs an input 13 times larger to predict the phase-shift. The other reason for the difference in convergence has to do with the complexity of the network, where the second model has approximately 5 million parameters to optimize, while the first is almost 5 times smaller.

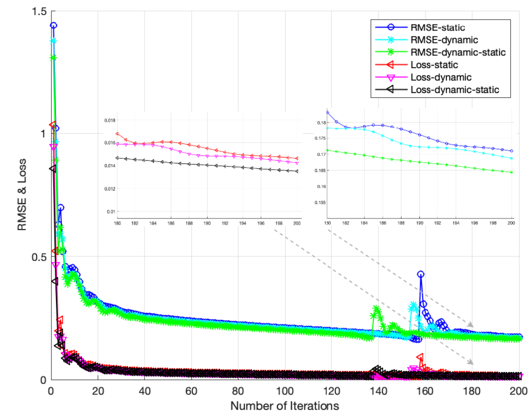

Fig. 5. RMSE and loss training results for trajectory model with the static and dynamic group movement.

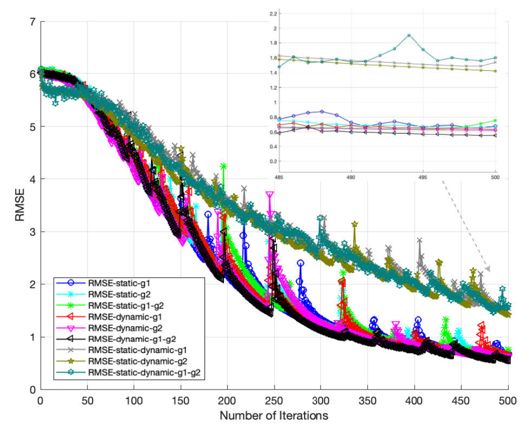

Fig. 6. RMSE and loss training results for phase-shift model with the static and dynamic group movement.

In terms of RMSE and Loss for the trajectory models, the static model has an RMSE of 0.171 with a training loss of 1.46%, the dynamic model has an RMSE of 0.168 with a training loss of 1.42% and the mix model (static and dynamic together) has an RMSE of 0.164 with a final loss of 1.35%. Although the results are very close, it is possible to recognize that the results of the model that uses static and dynamic information to predict the trajectory are better compared to the other 2 models in the training phase. This is due to the fact that the other 2 models were only trained with one type of data (either only static information or only dynamic information). In addition, it is also possible to observe the peaks in both figures due two possible reasons: the regularization put in place during the training phase (L2 regularization method) and the attempt to converge on a minimum (local or global).

As can be observed in Fig. 6, although both models (static, dynamic, and mix) converge throughout the training phase, it can be concluded that using both pieces of information (static and dynamic) to predict the phase-shift of the AIRS makes the model less effective at predicting it, having a RMSE higher than 1.4, while models that only use one type of information manage to be below 1 in RMSE. Concerning the models that only use one type of information, the results are quite close, but the dynamic model achieves better results.

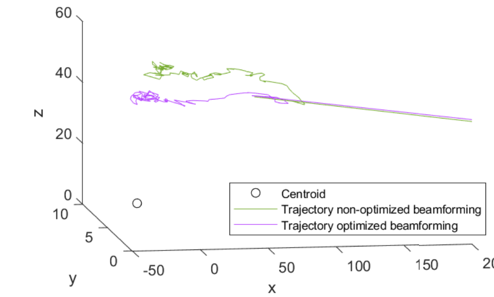

(a) Trajectory static scenario.

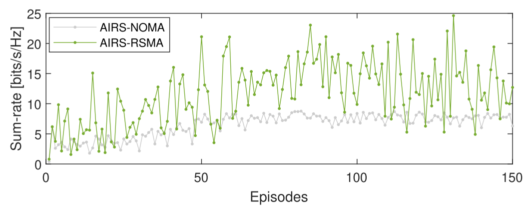

(b) Sum-rate for static scenario with non-optimized beamforming.

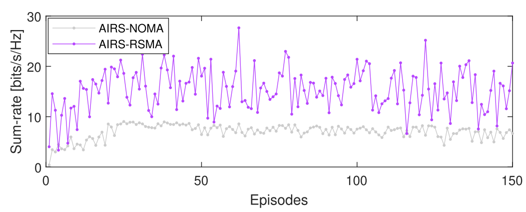

(c) Sum-rate for static scenario with optimized beamforming.

Fig. 7. Performance comparison static scenario with $\rho = 40$ dB and $\epsilon = 0.1$.

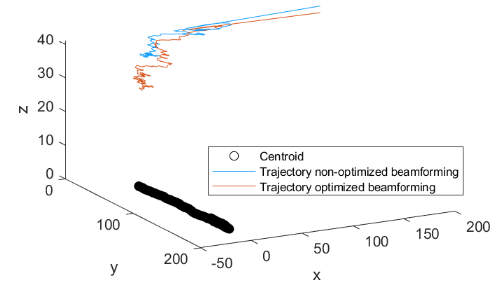

(a) Trajectory dynamic scenario.

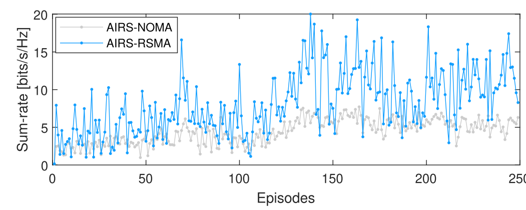

(b) Sum-rate for dynamic scenario with non-optimized beamforming.

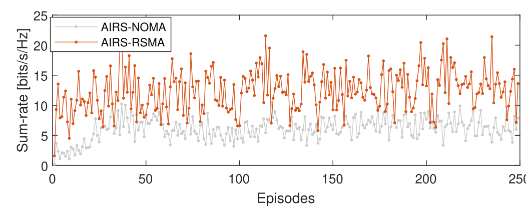

(c) Sum-rate for dynamic scenario with optimized beamforming.

Fig. 8. Performance comparison dynamic scenario with $\rho = 40$ dB and $\epsilon = 0.1$.

B. Performance Analysis

In order to demonstrate the potential of the proposed methods, this subsection provides testing and performance results for each investigated scenario. Fig. 7 depicts the trajectory of the UAV (Fig. 7a) and the sum-rate versus the episodes (Fig. 7b and Fig. 7c) in the proposed AIRS-RSMA network for a static scenario. The analysis considers both non-optimized, where a random precoder is used, and optimized beamforming approaches. For comparison, the AIRS-NOMA scheme is also plotted. The AIRS-NOMA scheme shows lower performance gains, as it is more susceptible to errors caused by imperfect SIC. In contrast, the AIRS-RSMA scheme can reduce and control decoding errors by adjusting the split of the common and private messages. By employing optimized beamforming, higher performance gains are achieved due to the capacity to redirect the signal, providing an adaptive beam between the BS and AIRS.

Fig. 8 shows the trajectory of the UAV (Fig. 8a) and the sum-rate versus the episodes (Fig. 8b and Fig. 8c) for a dynamic scenario, considering both optimized and non-optimized beamforming. It is evident that the application of optimized beamforming results in better and more stable rate gains throughout the episodes. Furthermore, in this scenario, the AIRS-RSMA network also outperforms the AIRS-NOMA.

Fig. 9 investigates the total sum-rate for the static scenario versus the transmit SNR. To compare the performance between the proposed DL methods, the joint dynamic-static (dyn-sta) and static (sta) models based on combining data from all user groups (g1-g2) are applied to predict the phase-shift (PS) and the trajectory (Traj) of the UAV. One can see that the static model achieves superior gains in terms of sum-rate when compared with dyn-sta model. In particular, when the SNR is 35 dB and $\epsilon = 0.1$, the static method achieves a performance of 23.7 bits/s/Hz, while dyn-sta can reach 20.1 bits/s/Hz. Since the combined model uses data from both static and dynamic scenarios, the UAV may follow a parabolic trajectory when it is not needed. Additionally, it is observed that the impact of the trajectory is greater than that of the phase-shift. This result is confirmed when the dyn-sta model is applied for PS optimization and the static model for trajectory optimization. In this case, the obtained sum-rate shows similar results to when the static model is used to predict both PS and trajectory.

Fig. 10 investigates the total sum-rate for the dynamic scenario versus the transmit SNR, in which the joint dyn-sta and dynamic models are applied. It is evident that the dynamic model outperforms the dyn-sta model. For instance, when the SNR is 35 dB and ϵ is 0.1, the dyn-sta method achieves a performance of 17.7 bits/s/Hz, while the dynamic model can reach 20.3 bits/s/Hz, representing a performance gain of approximately 12.8%. Additionally, it is observed that trajectory prediction also has a greater impact on the dynamic scenario.

In particular, by comparing the performance between Fig. 9 and Fig. 10, one can see that the static scenario achieves

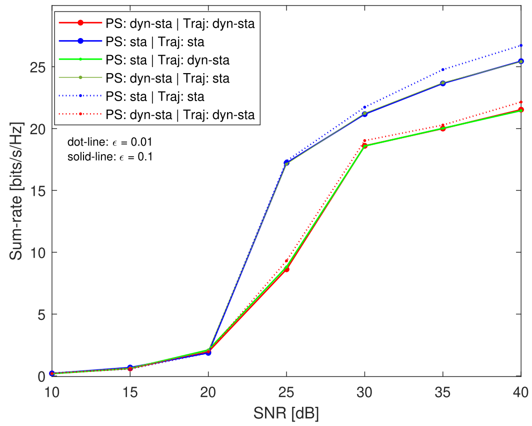

Fig. 9. Sum-rate for AIRS-RSMA scheme versus transmit SNR for static scenario with different prediction models.

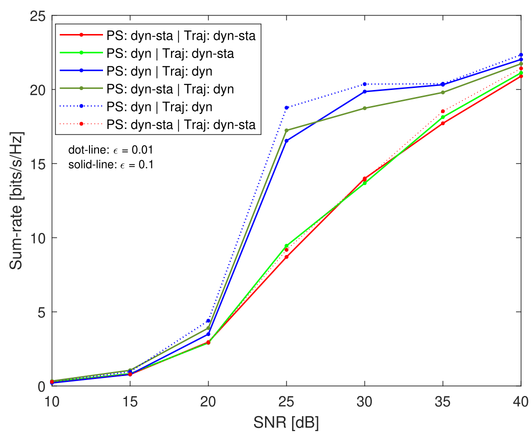

Fig. 10. Sum-rate for AIRS-RSMA scheme versus transmit SNR for dynamic scenario with different prediction models.

superior performance compared to the dynamic scenario. It is important to mention that the dynamic scenario represents the worst case. Additionally, the combined model (dyn-sta) achieves similar performance for both scenarios when the SNR is 40 dB. This is because the dyn-sta scheme is modeled by combining data from both scenarios, and the models were trained considering $\rho = 40$ dB. Note that it is possible to perform the training process for other values.

For a fair comparison, we compared the performance of the LSTM with the Gated Recurrent Unit (GRU) [48], commonly used in sequence modeling tasks. Despite their similarities, there are some differences between LSTM and GRU layers:

- LSTM has a more complex architecture compared to GRU: the input gate, forget gate, and output gate. Due to its more complex architecture, LSTM can potentially learn more complex patterns and relationships in the data. It is well-suited for tasks where capturing long-term dependencies is critical;
- GRU has a simplified architecture with two gates: the update gate and reset gate. While simpler, GRU can still learn to capture long-term dependencies effectively.

To validate the comparison of the two architectures, performance comparison were conducted as seen in Fig. 11 and Fig. 12

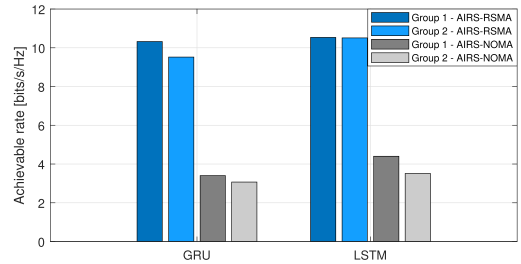

Fig. 11. Comparison of group rate fairness for different RNN structures in a static scenario. $\rho = 40$ dB, $\epsilon = 0.1$.

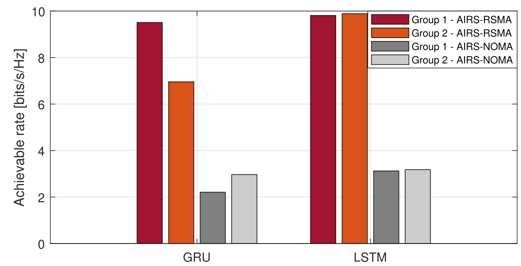

Fig. 12. Comparison of group rate fairness for different RNN structures in a dynamic scenario. $\rho = 40$ dB, $\epsilon = 0.1$.

Fig. 11 presents a performance comparison in terms of the achievable rate for each user group in the static scenario when the UAV reaches the shortest distance to the centroid of the user groups. The observation space used to train the LSTM is also for training the GRU. One can see that both techniques provide similar performance in terms of rate, which means both methods have been finding the centroid in a similar direction. However, the predicted trajectory by LSTM is more effective in terms of group rate fairness than the one provided by GRU.

Fig. 12 depicts a performance comparison in terms of the achievable rate for each user group in the dynamic scenario. One can see that the LSTM is able to identify the characteristics of the environment more efficiently and is more robust to the random nature of user movement. Additionally, the UAV follows a trajectory that aims to benefit both groups, resulting in better overall performance rates. On the other hand, the trajectory generated by the GRU provides lower rates and a lower fairness factor between the groups, demonstrating that the learning index of the GRU is lower than that of the LSTM.

VI. Conclusion

In this work, MISO-RSMA network with multiuser assisted by AIRS was investigated. We presented the system model and formulated the beamforming problem, along with its solution. Our focus was on enhancing the total achievable rate of the system by predicting environmental characteristics, including the trajectory of the UAV and the phase-shift of the AIRS elements. We constructed dynamic and static observation spaces based on real-time environmental features such as UAV position, phase-shift vectors maximizing the sum-rate of each group at the t-th time, and total system sum-rate. To yield more insightful results, we combined the dynamic and static models to create a third model. Subsequently, we tested the proposed models on the AIRS-RSMA network, presenting training, testing, and numerical results for each scenario, which showed improved sum-rate compared to non-optimized beamforming AIRS-RSMA and AIRS-NOMA schemes.

In addition, it has been validated that using static and dynamic information separately is more effective than combining them when predicting the next position in the trajectory and forecasting the phase-shift. Furthermore, it has been revealed that the trajectory has a more significant impact on the sum-rate than the phase-shift. The results also demonstrate that the combining model achieves similar performance for both scenarios.

APPENDIX

To verify if the solution for $\mathbf{P}_g$ satisfies the rank-one condition, we first investigate if the obtained solution satisfies the Karush-Kuhn-Tucker (KKT) conditions. To verify the KKT conditions, the Lagrangian function of problem (30a) is formulated following a similar approach provided in [39] and [49]. Without loss of generalization, the Lagrangian function of problem (30a) with respect to $\mathbf{P}_g^{c*}$ is given by

$$\begin{aligned}\mathcal{L}(\mathbf{P}_g^{c*}) = \sum_{k=1}^{K} \mu_{gk}^{*}[\rho \mathbf{h}_{gk}\mathbf{P}_g^{c*}\mathbf{h}_{gk}^{H}\alpha_g^{c}] \\ - \mathbf{P}_g^{c*}\mathbf{\Gamma}_c^{*} + \lambda^{*}[\mathbf{P}_c^{*} - P_{tot}],\end{aligned} \quad (39)$$

where μ^* and λ^* are the optimal dual variables associated with the constraint (30c) and (30e), respectively. Besides, Γ_c^* is the optimal dual variable matrix associated with constraint (30g). The KKT conditions of problem (30a) are expressed as

$$\begin{aligned}&\bar{C}1 : \mathbf{\Gamma}_c^{*} \succeq \mathbf{0}, \quad \bar{C}2 : \mathbf{P}_g^{c*}\mathbf{\Gamma}_c^{*} = \mathbf{0},\\ &\bar{C}3 : \mathbf{P}_g^{c*} \succeq \mathbf{0}, \quad \bar{C}4 : \lambda^{*}[\mathbf{P}_g^{c*} - P_{tot}] = 0.\end{aligned}$$

Taking partial derivate of $\mathcal{L}(\mathbf{P}_g^{c*})$ in (39) and applying the KKT conditions, we obtain

$$\bigtriangledown_{\mathbf{P}_g^{c*}}\mathcal{L}(\mathbf{P}_g^{c*}) = \sum_{k=1}^{K} \mu_{gk}^{*}[\rho \mathbf{h}_{gk}\mathbf{h}_{gk}^{H}\alpha_g^{c}] - \mathbf{\Gamma}_c^{*} + \lambda^{*}\mathbf{I}_N, \quad (40)$$

For $\bigtriangledown_{\mathbf{P}_g^{c*}}\mathcal{L}(\mathbf{P}_g^{c*}) = 0$, we obtain

$$\mathbf{\Gamma}_c^{*} = \lambda^{*}\mathbf{I}_N - \underbrace{\sum_{k=1}^{K} \mu_{gk}^{*}[\rho \mathbf{h}_{gk}\mathbf{h}_{gk}^{H}\alpha_g^{c}]}_{\mathbf{H}_g^{c*}}, \quad (41)$$

where $\mathbf{H}_g^{c*}$ is a Hermitian matrix. Since $\mathbf{\Gamma}_c^{*} = \lambda^{*}\mathbf{I}_N - \mathbf{H}_g^{c*} \succeq \mathbf{0}$ is positive semi-definite for KKT condition $\bar{C}1$, and $\lambda^{*} \geq \tilde{\lambda}_{\mathbf{H}_g^{c*}}^{\max} \geq 0$, in which $\tilde{\lambda}_{\mathbf{H}_g^{c*}}^{\max}$ is the maximum eigenvalue of $\mathbf{H}_g^{c*}$. From the condition $\bar{C}2$, since $\lambda^{*} > \tilde{\lambda}_{\mathbf{H}_g^{c*}}^{\max}$, $\mathbf{\Gamma}_c^{*}$ has a full rank. On the other hand, if $\lambda^{*} = \tilde{\lambda}_{\mathbf{H}_g^{c*}}^{\max}$ and $\mathrm{Rank}(\mathbf{\Gamma}_c^{*}) = N - 1$, we have $\mathrm{Rank}(\mathbf{P}_g^{c*}) = 1$. Similarly, it is possible to prove that the solution of $\mathbf{P}_{gk}^{p*}$, $\forall k \in \mathcal{K}$ and $\forall g \in \mathcal{G}$ is rank-one. ■

REFERENCES

[1] B. Clerckx, H. Joudeh, C. Hao, M. Dai, and B. Rassouli, "Rate splitting for MIMO wireless networks: A promising PHY-layer strategy for LTE evolution," *IEEE Commun. Mag.*, vol. 54, no. 5, pp. 98–105, May 2016.

[2] Y. Mao, B. Clerckx, and V. Li, "Rate-splitting multiple access for downlink communication systems: Bridging, generalizing and outperforming SDMA and NOMA," *EURASIP J. Wireless Commun. Net.*, vol. 2018, p. 133, May 2018.

[3] B. K. Lima, D. B. da Costa, L. Yang, F. R. M. Lima, R. Oliveira, and U. S. Dias, "Adaptive power factor allocation for cooperative full-duplex NOMA systems with imperfect SIC and rate fairness," *IEEE Trans. Veh. Technol.*, vol. 69, no. 11, pp. 14061–14066, Nov. 2020.

[4] Z. Yang, M. Chen, W. Saad, and M. Shikh-Bahaei, "Optimization of rate allocation and power control for rate splitting multiple access (RSMA)," *IEEE Trans. Commun.*, vol. 69, no. 9, pp. 5988–6002, Dec. 2021.

[5] X. Yuan, Y.-J. A. Zhang, Y. Shi, W. Yan, and H. Liu, "Reconfigurable-intelligent-surface empowered wireless communications: Challenges and opportunities," *IEEE Wireless Commun.*, vol. 28, no. 2, pp. 136–143, Apr. 2021.

[6] A. Bansal, K. Singh, B. Clerckx, C.-P. Li, and M.-S. Alouini, "Rate-splitting multiple access for intelligent reflecting surface aided multi-user communications," *IEEE Trans. Veh. Technol.*, vol. 70, no. 9, pp. 9217–9229, Aug. 2021.

[7] H. Fu, S. Feng, and D. W. K. Ng, "Resource allocation design for IRS-aided downlink MU-MISO RSMA systems," in *Proc. IEEE Int. Conf. Commun. Workshops (ICC Workshops)*, Jun. 2021, pp. 1–6.

[8] Z. Yang, J. Shi, Z. Li, M. Chen, W. Xu, and M. Shikh-Bahaei, "Energy efficient rate splitting multiple access (RSMA) with reconfigurable intelligent surface," in *Proc. IEEE Int. Conf. Commun. Workshops (ICC Workshops)*, Jun. 2020, pp. 1–6.

[9] A. Bansal, N. Agrawal, and K. Singh, "Rate-splitting multiple access for UAV-based RIS-enabled interference-limited vehicular communication system," *IEEE Trans. Intell. Vehicles*, vol. 8, no. 1, pp. 936–948, Jan. 2023.

[10] P. Liu, Y. Li, W. Cheng, X. Dong, and L. Dong, "Active intelligent reflecting surface aided RSMA for millimeter-wave hybrid antenna array," *IEEE Trans. Commun.*, vol. 71, no. 9, pp. 5287–5302, 2023, doi: 10.1109/TCOMM.2023.3285290.

[11] M. Katwe, K. Singh, B. Clerckx, and C.-P. Li, "Rate splitting multiple access for sum-rate maximization in IRS aided uplink communications," *IEEE Trans. Wireless Commun.*, vol. 22, no. 4, pp. 2246–2261, Apr. 2023.

[12] T. N. Do, G. Kaddoum, T. L. Nguyen, D. B. da Costa, and Z. J. Haas, "Aerial reconfigurable intelligent surface-aided wireless communication systems," in *Proc. IEEE 32nd Annu. Int. Symp. Pers., Indoor Mobile Radio Commun. (PIMRC)*, Sep. 2021, pp. 525–530.

[13] X. Pang, M. Sheng, N. Zhao, J. Tang, D. Niyato, and K. Wong, "When UAV meets IRS: Expanding air-ground networks via passive reflection," *IEEE Wireless Commun.*, vol. 28, no. 5, pp. 164–170, Oct. 2021.

[14] B. K. S. Lima et al., "Aerial intelligent reflecting surfaces in MIMO-NOMA networks: Fundamentals, potential achievements, and challenges," *IEEE Open J. Commun. Soc.*, vol. 3, pp. 1007–1024, 2022.

[15] S. Alfattani et al., "Aerial platforms with reconfigurable smart surfaces for 5G and beyond," *IEEE Commun. Mag.*, vol. 59, no. 1, pp. 96–102, Jan. 2021.

[16] X. Tang, H. He, L. Dong, L. Li, Q. Du, and Z. Han, "Robust secrecy via aerial reflection and jamming: Joint optimization of deployment and transmission," *IEEE Internet Things J.*, vol. 10, no. 14, pp. 12562–12576, Jul. 2023.

[17] S. K. Singh, K. Agrawal, K. Singh, B. Clerckx, and C.-P. Li, "RSMA enhanced RIS-FD-UAV-aided short packet communications under imperfect SIC," in *Proc. IEEE Globecom Workshops (GC Wkshps)*, 2022, pp. 1549–1554.

[18] S. Hochreiter and J. Schmidhuber, "Long short-term memory," *Neural Comput.*, vol. 9, no. 8, pp. 1735–1780, Nov. 1997.

[19] G. Gui, H. Huang, Y. Song, and H. Sari, "Deep learning for an effective nonorthogonal multiple access scheme," *IEEE Trans. Veh. Technol.*, vol. 67, no. 9, pp. 8440–8450, Sep. 2018.

[20] S. Kim, J. Son, and B. Shim, "Energy-efficient ultra-dense network using LSTM-based deep neural networks," *IEEE Trans. Wireless Commun.*, vol. 20, no. 7, pp. 4702–4715, Jul. 2021.

[21] A. K. Kowshik, A. H. Raghavendra, S. Gurugopinath, and S. Muhaidat, "Deep learning-based signal detection for rate-splitting multiple access under generalized Gaussian noise," *IEEE Open J. Veh. Technol.*, vol. 4, pp. 257–270, 2023.

[22] X. Gao, Y. Liu, X. Liu, and L. Song, "Machine learning empowered resource allocation in IRS aided MISO-NOMA networks," *IEEE Trans. Wireless Commun.*, vol. 21, no. 5, pp. 3478–3492, May 2022.

[23] X. Gao, X. Mu, W. Yi, and Y. Liu, "Intelligent trajectory design for RIS-NOMA aided multi-robot communications," *IEEE Trans. Wireless Commun.*, vol. 22, no. 11, pp. 7648–7662, 2023, doi: 10.1109/TWC.2023.3254130.

[24] C. Nguyen, T. M. Hoang, and A. A. Cheema, "Channel estimation using CNN-LSTM in RIS-NOMA assisted 6G network," *IEEE Trans. Mach. Learn. Commun. Netw.*, vol. 1, pp. 43–60, 2023.

[25] M. Wu, K. Guo, Z. Lin, X. Li, K. An, and Y. Huang, "Joint optimization design of RIS-assisted hybrid FSO SAGINs using deep reinforcement learning," *IEEE Trans. Veh. Technol.*, vol. 73, no. 3, pp. 3025–3040, 2024, doi: 10.1109/TVT.2023.3324970.

[26] X. Liu, Y. Deng, C. Han, and M. D. Renzo, "Learning-based prediction, rendering and transmission for interactive virtual reality in RIS-assisted terahertz networks," *IEEE J. Sel. Areas Commun.*, vol. 40, no. 2, pp. 710–724, Feb. 2022.

[27] K. D. Gupta, R. Nigam, D. K. Sharma, and S. K. Dhurandher, "LSTM-based energy-efficient wireless communication with reconfigurable intelligent surfaces," *IEEE Trans. Green Commun. Netw.*, vol. 6, no. 2, pp. 704–712, Jun. 2022.

[28] H. Kim, Y. Byun, and B. Shim, "LSTM-based RIS phase shift control for V2X communication systems," in *Proc. IEEE 96th Veh. Technol. Conf. (VTC-Fall)*, Sep. 2022, pp. 1–5.

[29] L. Yan, X. Fang, Y. Fang, L. Hao, Q. Xue, and C. Xu, "KF-LSTM based beam tracking for UAV-assisted mmWave HSR wireless networks," *IEEE Trans. Veh. Technol.*, vol. 71, no. 10, pp. 10796–10807, Oct. 2022.

[30] S. Zhang and R. Cao, "Multi-objective optimization for UAV-enabled wireless powered IoT networks: An LSTM-based deep reinforcement learning approach," *IEEE Commun. Lett.*, vol. 26, no. 12, pp. 3019–3023, Dec. 2022.

[31] F. Guo, L. Lu, Z. Zang, and M. Shikh-Bahaei, "Machine learning for predictive deployment of UAVs with multiple access," *IEEE Open J. Commun. Soc.*, vol. 4, pp. 908–921, 2023.

[32] R. Kant, P. Saini, and J. Kumari, "Long short-term memory auto-encoder-based position prediction model for fixed-wing UAV during communication failure," *IEEE Trans. Artif. Intell.*, vol. 4, no. 1, pp. 173–181, Feb. 2023.

[33] K. Li, W. Ni, and F. Dressler, "LSTM-characterized deep reinforcement learning for continuous flight control and resource allocation in UAV-assisted sensor network," *IEEE Internet Things J.*, vol. 9, no. 6, pp. 4179–4189, Mar. 2022.

[34] Y. Zhang, Z. Jia, C. Dong, Y. Liu, L. Zhang, and Q. Wu, "Recurrent LSTM-based UAV trajectory prediction with ADS-B information," in *Proc. IEEE Global Commun. Conf.*, Dec. 2022, pp. 1–6.

[35] S. K. Singh, K. Agrawal, K. Singh, B. Clerckx, and C.-P. Li, "RSMA for hybrid RIS-UAV-aided full-duplex communications with finite blocklength codes under imperfect SIC," *IEEE Trans. Wireless Commun.*, vol. 22, no. 9, pp. 5957–5975, 2023, doi: 10.1109/TWC.2023.3238808.

[36] B. K. S. Lima et al., "Rate-splitting multiple access networks assisted by aerial intelligent reflecting surfaces," in *Proc. IEEE Latin-American Conf. Commun. (LATINCOM)*, Nov. 2022, pp. 1–6.

[37] B. K. S. Lima, D. B. da Costa, R. Oliveira, R. Dinis, M. Beko, and U. S. Dias, "Power allocation, relay selection, and user pairing for cooperative NOMA systems with rate fairness," in *Proc. IEEE 93rd Veh. Technol. Conf. (VTC-Spring)*, Apr. 2021, pp. 1–5.

[38] C. You, B. Zheng, and R. Zhang, "Channel estimation and passive beamforming for intelligent reflecting surface: Discrete phase shift and progressive refinement," *IEEE J. Sel. Areas Commun.*, vol. 38, no. 11, pp. 2604–2620, Nov. 2020.

[39] R. Feng, Q. Li, Q. Zhang, and J. Qin, "Robust secure beamforming in MISO full-duplex two-way secure communications," *IEEE Trans. Veh. Technol.*, vol. 65, no. 1, pp. 408–414, Jan. 2016.

[40] I. Pólik and T. Terlaky, "Interior point methods for nonlinear optimization," in *Nonlinear Optimization* (Lecture Notes in Mathematics). Berlin, Germany: Springer-verlag, 1989, Jan. 2010.

[41] J. P. Matos-Carvalho, S. D. Correia, and S. Tomic, "Sensitivity analysis of LSTM networks for fall detection wearable sensors," in *Proc. 6th Conf. Cloud Internet Things (CIoT)*, Mar. 2023, pp. 112–118.

[42] R. Santos, J. P. Matos-Carvalho, S. Tomic, M. Beko, and S. D. Correia, "A hybrid LSTM-based neural network for satellite-less UAV navigation," in *Proc. 6th Conf. Cloud Internet Things (CIoT)*, Mar. 2023, pp. 91–97.

[43] R. Santos, J. P. Matos-Carvalho, S. Tomic, M. Beko, and S. D. Correia, "Applying deep neural networks to improve UAV navigation in satellite-less environments," in *Proc. Int. Young Engineers Forum (YEF-ECE)*, Jul. 2022, pp. 63–68.

[44] J. P. Matos-Carvalho, D. Pedro, L. M. Campos, J. M. Fonseca, and A. Mora, "Terrain classification using W-K filter and 3D navigation with static collision avoidance," in *Intelligent Systems and Applications*, Y. Bi, R. Bhatia, and S. Kapoor, Eds. Cham, Switzerland: Springer, 2020, pp. 1122–1137.

[45] R. Sacoto-Martins, J. Madeira, J. P. Matos-Carvalho, F. Azevedo, and L. M. Campos, "Multi-purpose low latency streaming using unmanned aerial vehicles," in *Proc. 12th Int. Symp. Commun. Syst., Netw. Digit. Signal Process. (CSNDSP)*, 2020, pp. 1–6.

[46] J. P. Matos-Carvalho, J. M. Fonseca, and A. Mora, "UAV downwash dynamic texture features for terrain classification on autonomous navigation," in *Proc. Federated Conf. Comput. Sci. Inf. Syst. (FedCSIS)*, Sep. 2018, pp. 1079–1083.

[47] A. S. de Sena et al., "Massive MIMO-NOMA networks with imperfect SIC: Design and fairness enhancement," *IEEE Trans. Wireless Commun.*, vol. 19, no. 9, pp. 6100–6115, Sep. 2020.

[48] K. Cho, B. Merrienboer, C. Gulcehre, F. Bougares, H. Schwenk, and Y. Bengio, "Learning phrase representations using RNN encoder–decoder for statistical machine translation," 2014, *arXiv:1406.1078*.

[49] H. Fu, S. Feng, W. Tang, and D. W. K. Ng, "Robust secure beamforming design for two-user downlink MISO rate-splitting systems," *IEEE Trans. Wireless Commun.*, vol. 19, no. 12, pp. 8351–8365, Dec. 2020.

Brena Kelly Sousa Lima received the B.Sc. degree in computer engineering and the M.Sc. degree in electrical and computer engineering from the Federal University of Ceará, Sobral, Brazil, in 2018 and 2020, respectively. She is currently pursuing the Ph.D. degree in computer science with Universidade Lusófona (UL), Lisbon, Portugal. She is also an invited Professor with UL and a Researcher with the Cognitive and People-Centric Computing (COPELABS), where she has been working in the wireless communication field. Her research interests include mobile communications, non-orthogonal multiple access techniques, intelligent reflecting surfaces, machine learning, and unmanned aerial vehicles (UAVs).

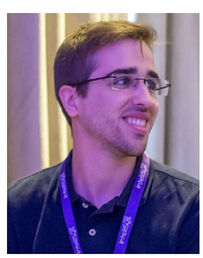

João Pedro Matos-Carvalho was born in Almada, Portugal, in 1993. He received the M.Sc. (Hons.) and Ph.D. degrees in electrical and computer engineering from FCT NOVA, Portugal, in 2017 and 2021, respectively. Since 2020, he has been an Integrated Member with the Center of Technology and Systems (CTS), UNINOVA, and COPELABS, Lusófona University. He is currently an Assistant Professor with Lusófona University. He has published more than 40 papers in international journals and international conferences in the field of remote sensing, pattern recognition, machine learning, sensor networks, and signal processing, with significant recognition and impact in the research community. He won the highly competitive Scientific Employment Stimulus (CEEC institutional) FCT grant in 2021. He received the Best Paper Award in a prestigious IEEE conference in 2018, the Distinguished Paper Award in 2021 by LASIGE at FCUL, and the Best Poster Presentation Award in 2023 by the International Complex Systems and Their Applications Conference. He has guest-edited three special issues entitled "Drone-Based Information Fusion to Improve Autonomous Navigation" (Drones), "UAV-Assisted IoT Solutions" (Drones), and "Territorial and Spatial-Based Simulation" (*Frontiers in Computer Science*), and serves as a reviewer for many prestigious scientific journals in his field. Since 2016, he has been working in the field of aerial robotics research and development.

Rui Dinis (Senior Member, IEEE) received the Ph.D. degree from the Instituto Superior Tècnico (IST), Technical University of Lisbon, Lisbon, Portugal, in 2001, and the Habilitation degree in telecommunications from Faculdade de Ciências e Tecnologia (FCT), Universidade Nova de Lisboa (UNL), Lisbon, in 2010. From 2001 to 2008, he was an Assistant Professor with IST. In 2003, he was an invited Researcher with Carleton University, Ottawa, ON, Canada. He was a Researcher with Centro de Análise e Processamento de Sinais, IST, from 1992 to 2005, and a Researcher with the Instituto de Sistemas e Robótica, from 2005 to 2008. Since 2009, he has been a Senior Researcher with the Instituto de Telecomunicações. He is currently a Full Professor with FCT–UNL. He has been actively involved in several national and international research projects in the broadband wireless communications area. His research interests include transmission, estimation, and detection techniques for wireless communications. He is a VTS Distinguished Speaker and a ComSoc Distinguished Lecturer. He is or was an Editor of IEEE TRANSACTIONS ON WIRELESS COMMUNICATIONS, IEEE TRANSACTIONS ON COMMUNICATIONS, IEEE TRANSACTIONS ON VEHICULAR TECHNOLOGY, IEEE OPEN JOURNAL OF THE COMMUNICATIONS SOCIETY, and *Physical Communication* (Elsevier). He was the guest editor of several special issues.

Marko Beko was born in Belgrade, Serbia, in November 1977. He received the Ph.D. degree in electrical and computer engineering from the Instituto Superior Técnico (IST), Universidade de Lisboa, Lisbon, Portugal, in 2008. He received the title of a "Professor with Habilitation" of electrical and computer engineering from the Universidade Nova de Lisboa, in 2018. He is one of the founders of Koala Tech. His research interests include signal processing for wireless communications. He is a member of the Editorial Board of IEEE OPEN JOURNAL OF VEHICULAR TECHNOLOGY. He was a recipient of the 2008 IBM Portugal Scientific Award. According to the methodology proposed by Stanford University, he was among the most influential researchers in the world from 2019 to 2022, when he joined the list of top 2% of scientists whose work is most cited by other colleagues in the field of information and communication technologies, sub-area networks and telecommunications. He is an Associate Editor of the IEEE OPEN JOURNAL OF THE COMMUNICATIONS SOCIETY.

Daniel Benevides da Costa (Senior Member, IEEE) received the B.Sc. degree in telecommunications from the Military Institute of Engineering (IME), Rio de Janeiro, Brazil, in 2003, and the M.Sc. and Ph.D. degrees in electrical engineering, area: telecommunications from the University of Campinas, Brazil, in 2006 and 2008, respectively. He is currently a Distinguished University Professor with the Department of Electrical Engineering, King Fahd University of Petroleum and Minerals (KFUPM), Saudi Arabia. His Ph.D. thesis was awarded the Best Ph.D. Thesis in Electrical Engineering by Brazilian Ministry of Education (CAPES) at the 2009 CAPES Thesis Contest. He was recognized as the World's Top 2% Scientist by Stanford University (2021, 2022, and 2023) and has been ranked among 1% Top Scientists in the world in the broad field of electronics and electrical engineering in 2022 and 2023. He is also a Distinguished Speaker of the IEEE Vehicular Technology Society. He is the Editor-in-Chief of the IEEE COMMUNICATIONS LETTERS.

Rodolfo Oliveira (Senior Member, IEEE) received the Licenciatura degree in electrical engineering from the Faculdade de Ciências e Tecnologia (FCT), Universidade Nova de Lisboa (UNL), Lisbon, Portugal, in 2000, the M.Sc. degree in electrical and computer engineering from the Instituto Superior Técnico, Technical University of Lisbon, in 2003, and the Ph.D. degree in electrical engineering from UNL, in 2009. From 2007 to 2008, he was a Visiting Researcher with the University of Thessaly. From 2011 to 2023, he was a Visiting Scholar with Carnegie Mellon University. He is currently with the Department of Electrical and Computer Engineering, UNL, and also a Senior Researcher with the Instituto de Telecomunicações, where he researches in the areas of wireless communications, computer networks, and computer science. He serves on the Editorial Board of *Ad Hoc Networks* (Elsevier), *ITU Journal on Future and Evolving Technologies* (ITU J-FET), IEEE OPEN JOURNAL OF THE COMMUNICATIONS SOCIETY, and IEEE COMMUNICATIONS LETTERS.